JOURNAL OF AIRCRAFT
Vol. 35, No. 6, November–December 1998

Navier–Stokes Analysis of the Flow About a Flap Edge

Donovan L. Mathias*
California Polytechnic State University, San Luis Obispo, California 93407
Karlin R. Roth,† James C. Ross,‡ and Stuart E. Rogers§
NASA Ames Research Center, Moffett Field, California 94035
and
Russell M. Cummings¶
California Polytechnic State University, San Luis Obispo, California 93407

The current study computationally examines one of the principal three-dimensional features of the flow over a high-lift system, the flow associated with a flap edge. Structured, overset grids were used in conjunction with an incompressible Navier–Stokes solver to compute the flow over a two-element high-lift configuration. The computations were run in a fully turbulent mode using the one-equation Baldwin–Barth model. Specific emphasis was given to the details of the flow in the vicinity of the flap edge, and so the geometry was simplified to isolate this region. The geometry consisted of an unswept wing, which spanned a wind-tunnel test section, equipped with a single-element flap. Two flap configurations were computed: a full-span and a half-span Fowler flap. The chord-based Reynolds number was 3.7×10^6 for all cases. The results for the full-span flap agreed with two-dimensional experimental results and verified the method. Grid topologies and related issues for the half-span flap geometry are discussed. Results of the half-span flap case are compared with three-dimensional experimental results, with emphasis on the flow features associated with the flap edge. The results show the effect of the vortex created by the flap edge, including the impact on flow separation and spanwise lift distribution.

Nomenclature

b = wingspan
C_l = section lift coefficient, $l/q_\infty c$
C_p = pressure coefficient, $(p - p_\infty)/q_\infty$
c = unflapped airfoil reference chord, 2.5 ft
l = sectional lift force
M = Mach number
p = static pressure
q = dynamic pressure, $\frac{1}{2}\rho V^2$
Re_c = Reynolds number, Vc/υ
V = flow velocity
x = chordwise position
y^+ = boundary-layer wall units
α = angle of attack, deg
β = artificial compressibility factor
δ_f = flap deflection angle, deg
ρ = fluid density
υ = fluid kinematic viscosity
∞ = freestream conditions

Introduction

HIGH-lift aerodynamics continues to be an important area of research because of the powerful effect high-lift systems have on the overall design of an aircraft.[1,2] Future improvements in high-lift system performance will most likely result from a better understanding of the driving flow physics. A number of previous authors have identified key flow features that influence high-lift flows, such as viscous wake interaction, confluent wakes and boundary layers, and separated flows.[2–4] Any attempt to study high-lift flows should possess the ability to resolve these viscous features. The need for viscous simulation, coupled with the relative success of two-dimensional computational fluid dynamics (CFD) methods,[5–8] suggested a computational approach for this investigation of a simple three-dimensional high-lift system.

The goal of this study was to use current computational tools to investigate one aspect of a three-dimensional high-lift system, namely the effect of a flap edge. A simple geometry was selected so that the flap-edge effects could be isolated from additional complications of real high-lift systems, such as sweep, fuselage interference, and wingtip effects. Takeoff and landing configurations for full- and half-span flap geometries were computed, but only the landing results are presented here. Grid issues important to resolving the flow about a flap edge in an efficient manner are also discussed. A complete discussion of both cases can be found in Refs. 9 and 10.

Geometry and Flow Conditions

Both of the geometries studied were based on the NACA 63_2-215 Mod. B airfoil section.[11] This airfoil was fitted with two riggings of a 30% chord Fowler flap representative of takeoff and landing configurations; Fig. 1 shows the airfoil with the landing flap rigging. The gap is defined as the vertical distance between the lower surface of the trailing edge and the highest point on the deflected flap element. Overlap is the horizontal distance between the main-element trailing edge and the leading edge of the deflected flap. All of the results presented are for a Reynolds number of $Re_c = 3.7 \times 10^6$ and an angle of attack of $\alpha = 10$ deg.

For the full-span case, the takeoff airfoil configuration was extruded into a wing that fully spanned a wind-tunnel test sec-

Presented as Paper 95-0185 at the AIAA 33rd Aerospace Sciences Meeting, Reno, NV, Jan. 9–12, 1995; received April 21, 1998; revision received June 8, 1998; accepted for publication July 9, 1998.

*Graduate Research Assistant, Aeronautical Engineering Department; currently Research Scientist, MCAT, Inc., Moffett Field, CA 94035. Student Member AIAA.

†Aerospace Engineer, Aerodynamics Directorate. Member AIAA.

‡Aerospace Engineer, Aerodynamics Directorate. Senior Member AIAA.

§Aerospace Engineer, Computational Algorithms and Applications Branch. Senior Member AIAA.

¶Professor, Aeronautical Engineering Department. Associate Fellow AIAA.

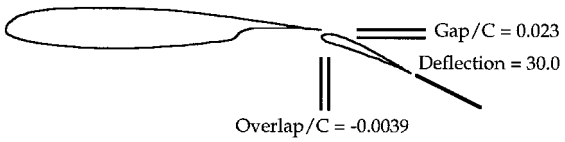

Fig. 1 NACA 63_2-215 Mod. B airfoil with 30% Fowler flap in landing configuration.

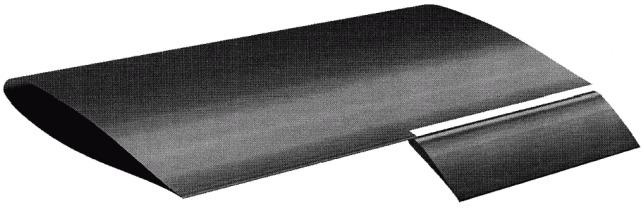

Fig. 2 Half-span flap geometry.

tion. The test section was modeled after the NASA Ames 7- by 10-ft Wind Tunnel in which the experiments were conducted.[12] False walls were present in the test section for model-mounting purposes (similar to those described in Ref. 13), and so the effective size of the test section was reduced to 5 × 10 ft. The wing was positioned such that it spanned the smaller dimension, which was two chords in length. The half-span flap geometry had a flapped airfoil that only extended over half of the tunnel span, whereas the unflapped section composed the second half of the span (Fig. 2).

Numerical Investigation

Flow Solver

The incompressible Navier–Stokes upwind differenced (INS3D-UP) flow solver was used to compute all of the solutions in this work.[14,15] Because the experimental freestream Mach number was low ($M_\infty = 0.2$), the exclusion of compressible effects was felt to be a minor sacrifice compared with the efficiency gained by using an incompressible code. INS3D-UP utilizes the method of artificial compressibility[16] to directly couple the velocity and pressure fields by adding a pressure fluctuation term to the continuity equation. The hyperbolic nature of the resulting equations can then be exploited through the use of an upwind differencing scheme. In this case, the convective flux terms are differenced with a flux-difference splitting scheme based on the method of Roe,[17] and the viscous fluxes are discretized using a standard, central-difference formulation. A Gauss-Seidel-type implicit line relaxation scheme is used to solve the system of equations.

Turbulence Model

The Baldwin–Barth turbulence model[18] was used for all of the computed cases. It has been shown by a number of researchers that this model does a reasonable job in predicting multielement airfoil flows.[7,8,19] All of the current cases were run in a fully turbulent mode, with no modeling of transition. The lack of transition modeling did not adversely affect the comparison with experimental data because transition strips were placed on the upper ($x/c = 0.10$) and lower ($x/c = 0.15$) surfaces of the main element in the experiment.

Computational Grids

Structured, overset grids were used throughout this study, taking advantage of the Chimera scheme.[20,21] Three zones were required to model the full-span flap geometry with a total of 900,000 grid points: the main wing element (227 × 30 × 80 in the nominally streamwise, spanwise, and normal directions, respectively), the flap element (155 × 30 × 59), and the wind-tunnel test section (85 × 30 × 30). For the half-span flap simulation, six grid zones were used with a total of 1.7 million grid points: the flapped main element (227 × 40 × 80), the unflapped main element (185 × 40 × 52), the flap element (155 × 40 × 59), the wind-tunnel test section, and two zones that represent the flap edge and the edge of the cove on the main element.

A C–H grid topology was used for all of the airfoil grids, based on the two-dimensional grids developed by Carrannanto et al.[7] For all of the C–H grids the wall spacing was 10^{-5} chords ($y^+_{av} \approx 1$), and the circumferential spacing at the trailing edge was 10^{-3} chords. The three other zones originated as two-dimensional H-grids and were stacked in the spanwise direction. The test section was modeled as a constant area duct, which extended ±15 chords from the leading edge of the main wing element. Because the wind-tunnel walls were modeled as inviscid surfaces, the slight divergence of the tunnel designed to account for boundary-layer growth was neglected. The grid used to model the end surface of the flap was a 36 × 10 × 40 stacked H-grid deformed to match the flat flap edge, while the grid used to model the exposed cove area at the junction of the flapped and unflapped main element sections was a 33 × 10 × 33 stacked H-grid (the exposed cove region at the flap edge is shown in Fig. 3).

The two-dimensional planes were copied and stacked together in the spanwise direction to form a three-dimensional grid prior to the merging of the zones. This allowed for different spanwise resolutions in each zone based on the requirements of each grid. By first working in two dimensions, most of the Chimera details could be worked out prior to creating the three-dimensional grid, saving both time and computer resources. The full-span flap grid was a direct extension of the two-dimensional case because all of the grid cross sections were identical. The number of spanwise planes was determined by end-spacing requirements and acceptable limits on stretching ratios (<1.3). The three-dimensional grids were then merged using Chimera concepts, where the interpolation links between the zones were established.[21]

Proper Chimera interpolation between grids proved a challenge in two locations, the overlap region between the flapped and unflapped main elements and the flap-edge region. The midspan location was complicated because two grids of different shapes were required to fit together and communicate. As mentioned, the shape difference between the two main-element sections was corrected through the use of the patch grid. The first spanwise plane of the patch grid was located at the solid surface, coincident with an unflapped grid plane, and the grid was continued 1.5×10^{-3} chords into the flapped portion of the grid. The interpolation between the flapped and unflapped main element grids was more difficult to establish. The unflapped main element extended 10^{-3} chords and four grid planes into the flapped element grid. This overlap allowed the end planes of each grid to receive interpolated information from the interior of the other grid. However, this overlap created an additional problem. The interior surface of a C-grid is a computational boundary and requires boundary information for a well-posed problem to exist. For the most part, the

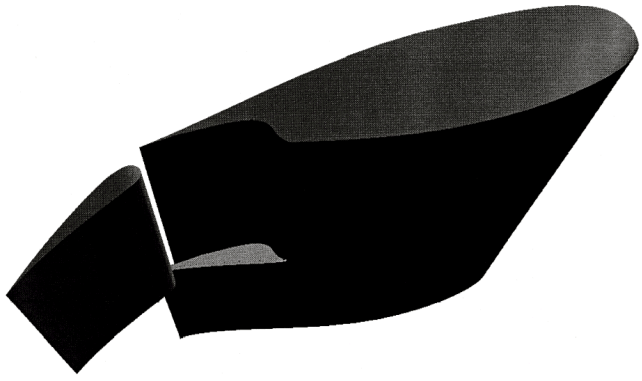

Fig. 3 Geometry of flap-edge cove region.

flapped and unflapped surfaces were coincident, and so solid surface boundary conditions could be used. Near the trailing edge this approach did not work because a portion of the flowfield in one grid (flapped main element) would have coincided with a solid surface in the other grid (unflapped main element). This would have created an inconsistency in the solution: the solver would be computing points inside a solid body. To circumvent this, the portion of the unflapped trailing edge that extended into the computational domain of the flapped grid was defined as a Chimera boundary and, thus, was updated by interpolation.

The interpolation stencils in the flap-edge region were simpler to set up, but turned out to play an important role in the convergence of the solution. The first approach was to place the last grid plane of the flap-edge grid at the solid surface and march the grid away from the surface as was done with the patch grid. Using this grid scheme, the solution would not converge. The convergence difficulty was traced to an unsteady flow separation occurring at the corner of the flap edge and flap surface near the leading edge. The flap-edge grid was not able to resolve this feature with only the grid boundary information provided by the Chimera scheme. The problem was fixed by extending the flap-edge grid three grid planes into the flap surface. The points inside the surface were blanked from the computational domain, and the flap-edge surface was formed by the third-from-the-last grid plane. This placed the flow separation completely inside the flap-edge grid, and the solution converged.

A grid resolution study for the full-span flap case was performed and is presented in Ref. 9. The grids used in this study were created based on the full-span flap grid resolution study. No grid resolution study was performed for the half-span grid because of the excessive computational requirements for a single solution. Because the solution exhibited small-scale flow features, such as secondary separation at the flap edge, the resolution in the region of interest appeared sufficient for this study. Figures 4 and 5 show cross sections of the resulting flapped and unflapped portions of the half-span flap grid.

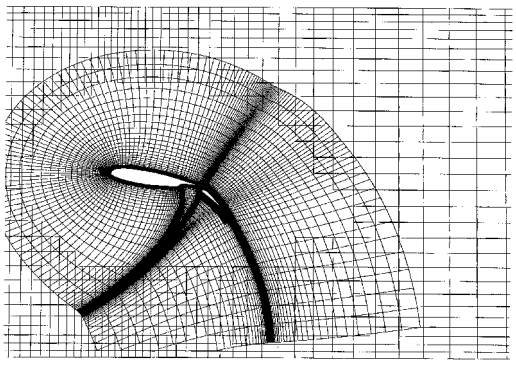

Fig. 4 Flapped airfoil grid cross section (including hole-cut boundaries in the outer grid).

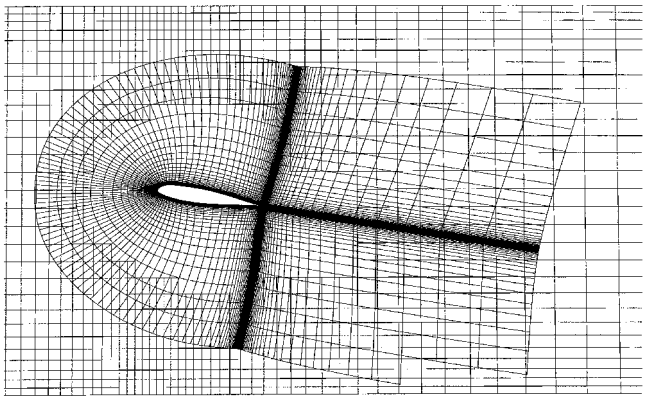

Fig. 5 Unflapped airfoil grid cross section (including hole-cut boundaries in the outer grid).

Boundary Conditions

All of the solid surface points on the wing were modeled using a no-slip boundary condition. This condition specifies zero velocity and a zero normal pressure gradient at the surface. Because a C-grid topology was used, wake-cut boundary conditions were also needed. Wake-cut boundary points were updated by a first-order averaging of the points on either side of the wake cut. The wind-tunnel walls were represented by slip-walls, which impose a zero normal gradient for all flow variables. The tunnel inflow condition was prescribed with uniform normal velocity and constant total pressure. The outflow of the tunnel consists of a constant static pressure and extrapolated velocity. The outer boundaries of all grid zones falling inside the wind-tunnel grid were Chimera boundaries.

Results and Discussion

Full-Span Flap

The flow for the full-span flap case was computed in a nontime accurate fashion with $\beta = 100$, which required 600 iterations and 12 CPU hours to converge. Figure 6 shows a comparison between computed and experimental pressure distributions for the full-span flap case. The results agree very closely over most of the chord. Some disagreement exists at the leading edge of the main element and the trailing edge of the flap. The difference at the trailing edge is probably because of the experimental model having a finite thickness trailing edge, whereas the computational trailing edge has no thickness. The full-span flap configuration was also used to study the spanwise grid sensitivity. The computed flows, however, turned out to be two dimensional and showed negligible sensitivity to spanwise grid density. Additional details for this case can be found in Refs. 9 and 10.

Half-Span Flap

The half-span flap configuration flow was computed to analyze the effects of the flap edge on the surrounding flowfield. Convergence in this case required 500 iterations and 20 CPU hours with $\beta = 100$. Figure 7 shows particle traces colored by the local value of static pressure, which provides a qualitative view of the large-scale flow features. This figure illustrates the location of the tip vortex as it forms and convects downstream. Also, large amounts of spanwise flow are seen on the flap and the unflapped main element. On both surfaces the flow moves toward the flap edge as a result of the velocities induced by the flap-edge vortex. Separation lines are also visible on both of these wing elements. The separation lines are in their most

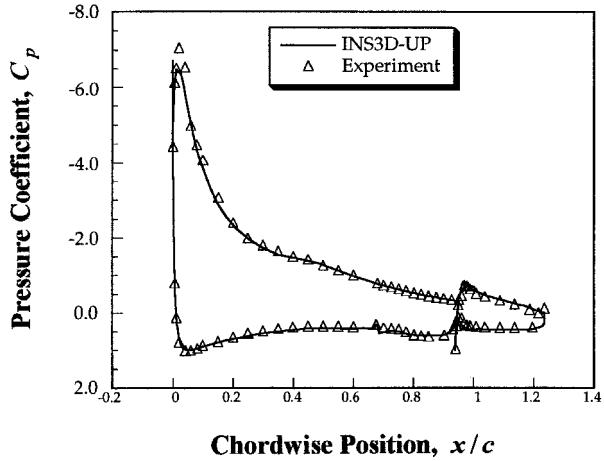

Fig. 6 Experimental and computational full-span flap pressure distributions. $\delta_f = 30$ deg, $\alpha = 10$ deg.

forward position at the outer edges of the wing and shift aft toward the midspan of the wing.

An enlarged view of the surface particle traces on the flap element is shown in Fig. 8. The separation line computed in a two-dimensional simulation of the same airfoil is indicated on the flap surface. At the wall the two separation points agree very closely, but by the midspan of the flap the three-dimensional separation point has shifted noticeably aft of the two-dimensional point. In the vicinity of the flap edge, the separation has all but been eliminated as a result of the pressure relief at the flap edge. Instead of maintaining strong chordwise pressure gradients at the edge, the flow moves around the edge, reducing the pressure gradients in this region. The streamlines that begin moving away from the flap edge, and then change direction and move toward the edge, indicate the formation of the tip vortex. As this flow negotiates the corner it separates and forms a small recirculating region of high-vorticity fluid, which is the beginning of the flap-tip vortex. As the vortex convects downstream, it is fed by the shear layer separating from the lower surface of the flap edge, which rolls up into the trailing vortex. Once the vortex has formed it remains above the upper surface of the flap all the way to the trailing edge. The vortex induces a velocity beneath it toward the flap edge, and the streamlines move in this direction over the aft half of the flap.

Similar results can be seen in Fig. 9 for the unflapped main element, with the two-dimensional separation line indicated for comparison. The spanwise flow is away from the wall toward the wing midspan in the direction induced by the flap-tip vortex. The magnitude of the spanwise flow is greatest at the midspan of the wing and decreases as the distance from the vortex increases. As with the flap, the separation line is farther aft near the midspan than at the wall. The position of the separation line moves in this case because of the presence of the free edge at the junction between the flapped and unflapped sections of the wing. This free edge allows relief of the pressure gradients, as was the case with the flap edge. The separation line near the wall is upstream of the two-dimensional position because of the upwash induced by the flap-tip vortex.

Particle traces restricted to the surface of the flap tip are shown in Fig. 10. Two interesting flow features are seen near the leading edge: a standing recirculation zone and a reattachment line. The recirculation zone is fed by spanwise flow separating from the flap surface. Above the recirculation zone an attachment line is visible that travels along the flap edge toward the upper surface of the flap. The flow then separates over the upper flap edge and rolls up into the beginning of the vortex core. The curvature of the particle traces near the lower portion of the flap edge is caused by the presence of another small recirculation zone, which is fed by spanwise flow leaving the lower surface of the flap.

Figure 11 contains a plot of the lift distribution for the half-span flap case. A sharp change in lift coefficient ($\Delta C_l = 0.3$) is visible at the edge of the flap element. The section lift coefficient for the same two-dimensional airfoil at $\alpha = 10$ deg is also shown. The three-dimensional lift is much lower than in two dimensions on the flapped portion of the wing and much

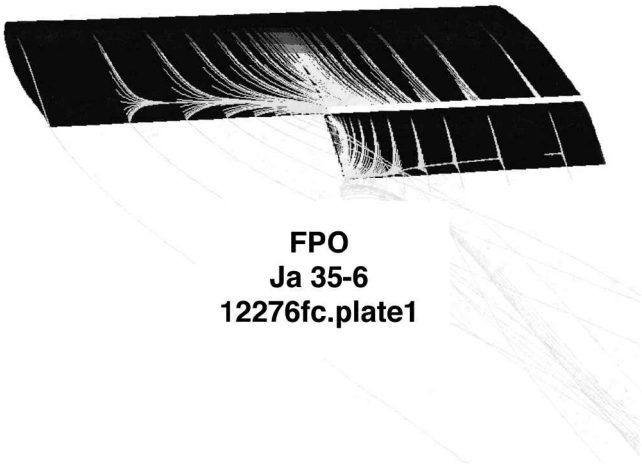

Fig. 7 Particle traces colored by static pressure.

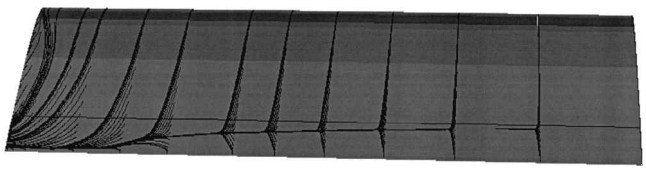

Fig. 8 Flap surface particle traces for half-span flap geometry. $\delta_f = 30$ deg, $\alpha = 10$ deg.

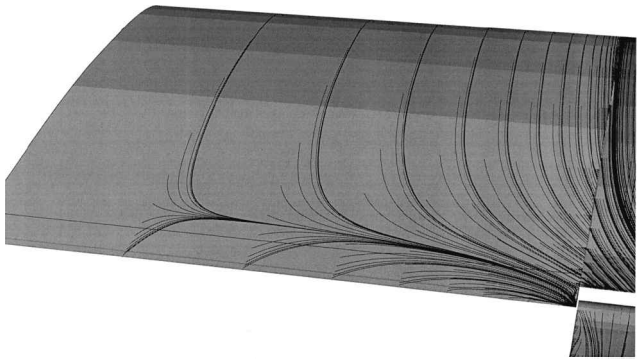

Fig. 9 Unflapped main element surface particle traces for half-span flap geometry. $\delta_f = 30$ deg, $\alpha = 10$ deg.

Fig. 10 Surface particle traces on the flap end. $\delta_f = 30$ deg, $\alpha = 10$ deg.

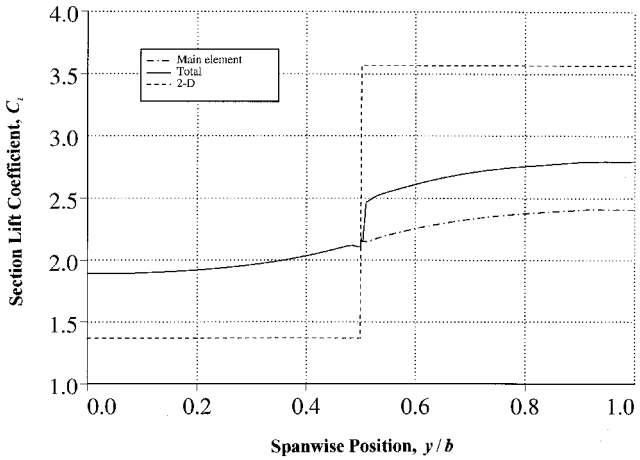

Fig. 11 Lift distribution, $\delta_f = 30$ deg, $\alpha = 10$ deg.

higher on the unflapped portion of the wing. This is not surprising because of the powerful effect the flap-edge vortex has on the surrounding flowfield. The trailing vortex induces an upwash on the unflapped half of the wing, whereas a downwash is induced on the flapped half-span. The local angle of attack is increased over the unflapped section and decreased over the flapped section; the magnitude of the angle change is greatest near the flap edge, i.e., nearest the vortex. The effect of the flap-edge vortex is apparent for the unflapped half of the wing as the lift increases from its lowest value at the wall to its highest value at the flap edge. The reverse effect is apparent for the flapped half of the wing, where the lift increases from its lowest value at the flap edge to its highest value near the wall.

Surface pressure plots can be used to quantitatively analyze the flowfield. Chordwise pressure distributions at varying spanwise positions are particularly useful in illustrating changes in the flow across the span of the wing. Figure 12 contains pressure distributions for two spanwise stations on the unflapped main element. The increased upwash nearest the flap edge, i.e., tunnel midspan, has increased the effective angle of attack compared to the section near the wall, decreasing the suction on the upper surface of the wing. A slight increase in the lower surface pressure coefficients at midspan can also be seen. The most significant difference between the two pressure distributions shown in Fig. 12 occurs in the vicinity of the trailing edge. The section near the flap edge displays a slightly favorable pressure gradient at the trailing edge, while the section near the wall shows continuing pressure recovery all the way to the trailing edge. This can be explained by the high induced velocities at the trailing edge of the midspan section. These induced velocities create a region of increased dumping velocity (the velocity that the flow leaving the trailing edge must adjust to), decreasing the amount that the pressure must recover. For an airfoil without a flap, the trailing-edge condition is such that the flow tends toward freestream as it leaves the airfoil surface. On a multielement airfoil, the flow leaving the trailing edge of an upstream element often has the tendency to approach a velocity much higher than freestream because of the high velocities induced by the downstream element. The unflapped portion of the wing is more susceptible to this phenomena because of the exposed edge created by the mismatch in chord at the junction of the flapped and unflapped sections. In all cases, the pressure distributions for sections between the midspan and the wall fall between the two curves shown in Fig. 12.

Figure 13 shows a similar plot for the flapped main element section. In this case, the upper surface pressure coefficients become more negative and the lower surface pressure coefficients become more positive away from the midspan. As with the unflapped section, the largest differences are seen at the trailing edge. No upturn in the pressure distribution is seen at the trailing edge of the midspan section in this case, because the upper surface velocities at the flapped trailing edge must match the velocities on the upper surface of the unflapped portion of the wing. The upper surface pressures must adjust so that they are continuous across the junction between the flapped and unflapped sections. Also, the lower surface of the flapped trailing edge is perpendicular to the solid surface formed by the patch grid because the flapped chord is 5% shorter than the unflapped chord. This solid surface allows a pressure difference between the upper and lower surfaces upstream of the trailing edge. Away from the midspan, the pressure distribution quickly begins to match the distribution at the wall.

The greatest spanwise variation of pressure distributions occurs on the flap element. Figure 14 shows pressure distributions at the flap edge and at the wall. At the flap edge the flow is dominated by the tip vortex, which completely alters the shape of the distribution. As shown in the plot, the leading-edge suction peak is suppressed at the flap edge because of the spanwise flow mentioned earlier. Away from the edge, the flow accelerates around the airfoil leading edge as it moves away from the attachment line, and the suction peak strengthens. As seen in Fig. 14, the peak has nearly reached the wall value at a distance of 0.1 chords from the edge. The velocities over the aft part of the airfoil's upper surface are higher at the edge than near the wall because of the presence of the tip

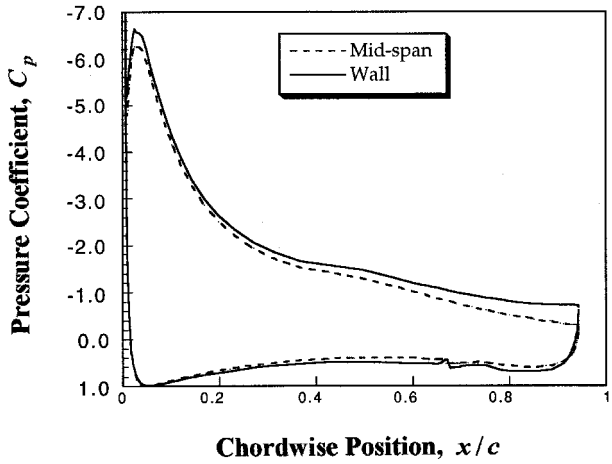

Fig. 13 Pressure distribution for two spanwise locations on flapped main element, $\delta_f = 30$ deg, $\alpha = 10$ deg.

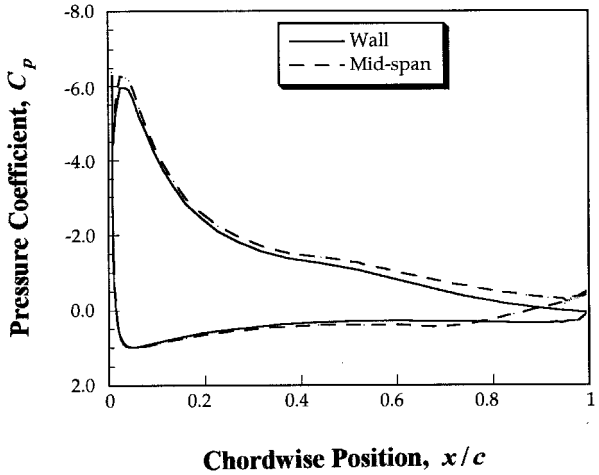

Fig. 12 Pressure distribution for two spanwise locations on unflapped main element, $\delta_f = 30$ deg, $\alpha = 10$ deg.

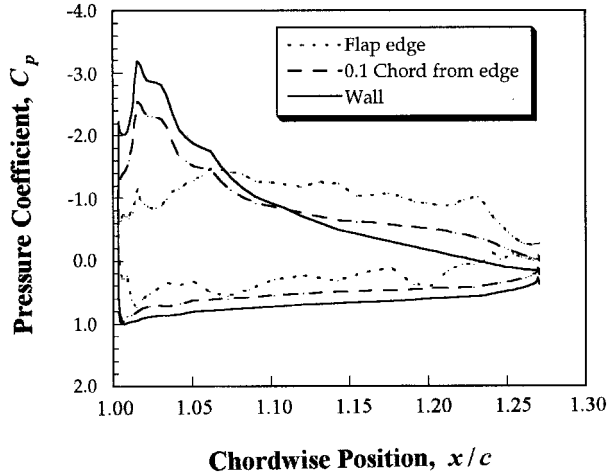

Fig. 14 Pressure distribution for three spanwise locations on flap element, $\delta_f = 30$ deg, $\alpha = 10$ deg.

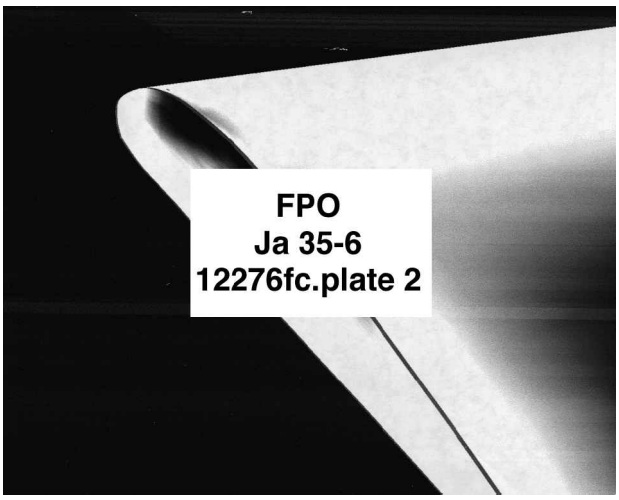

Fig. 15 Flap surface colored by static pressure.

vortex. The vortex travels just above the upper surface, inducing a region of high-speed flow beneath it. The high velocities are illustrated by the reduced pressure coefficients over much of the aft part of the flap upper surface.

Figure 15 shows the flap end colored by static pressure. This figure provides another visualization of many of the flow features discussed so far. For example, the dark red region near the leading edge indicates the low pressures and high velocities present in the recirculation zone caused by the spanwise flow separating from the flap edge. The large blue and green area along the upper surface shows higher pressures because of the reattachment line shown in Fig. 10. The spanwise pressure relief provided by the flap edge can also be seen here. On the most forward portion of the flap shown, the red color becomes darker away from the flap edge, which is bright yellow. The red tones indicate higher velocities and more suction. The edge also relieves the pressure gradients over the aft portion of the flap, as evidenced by the elimination of the green separated region close to the edge.

Conclusions

A computational investigation of the flow about a simple, three-dimensional high-lift system was performed. The computational approach was validated by investigating a flapped wing that spanned a wind-tunnel test section and comparing the results to experimental data. A wing with a half-span flap was also compared with experimental data to quantify the effects of a flap edge on the surrounding flowfield. This portion of the research included developing a grid scheme that would adequately resolve the flow in the vicinity of the flap edge. The study was successful in that it provided insight into the flow patterns on and near the flap edge. The features identified in this work suggest flow features to look for in future experimental and computational studies of high-lift systems. These features include the formation and effects of the flap-edge vortex, including the impact on flow separation and spanwise lift distribution. The flap-edge vortex changes the downwash/upwash field in the vicinity of the flap edge, which adversely impacts flow separation on the unflapped wing element. The lift distribution in the vicinity of the flap is also adversely affected by the flap-edge vortex. These effects suggest the importance of understanding the flow in the flap-edge region in the design of three-dimensional flap systems.

Acknowledgments

This research was funded by NASA Ames Research Center Cooperative Agreement NCC 2-813. The computing time for this work was provided by the Numerical Aerodynamic Simulation (NAS) System at NASA Ames Research Center.

References

[1]Dillner, B., May, F. W., and McMasters, J. H., "Aerodynamic Issues in the Design of High-Lift Systems for Transport Aircraft," AGARD, CP-365, Aug. 1984 (Paper 9).

[2]Meredith, P. T., "Viscous Phenomena Affecting High-Lift Systems and Suggestions for Future CFD Development," AGARD, CP-515, Oct. 1992 (Paper 19).

[3]Valarezo, W. O., Dominik, C. J., and McGhee, R. J., "Reynolds and Mach Number Effects on Multielement Airfoils," *Proceedings of the 5th Numerical and Physical Aspects of Aerodynamic Flows*, California State Univ., Long Beach, CA, Jan. 1992.

[4]Woodward, D. S., Hardy, B. C., and Ashill, P. R., "Some Types of Scale Effects in Low-Speed, High-Lift Flows," *Proceedings of the 16th ICAS Congress* (Jerusalem, Israel), AIAA, Washington, DC, 1988, pp. 1402–1416.

[5]Rogers, S. E., "Progress in High-Lift Aerodynamic Calculations," AIAA Paper 93-0194, Jan. 1993.

[6]Rogers, S. E., "Efficient Simulation of Incompressible Viscous Flow over Single and Multi-Element Airfoils," AIAA Paper 92-0405, Jan. 1992.

[7]Carrannanto, P. C., Storms, B. L., Ross, J. C., and Cummings, R. M., "Navier-Stokes Analysis of Lift-Enhancing Tabs on Multi-Element Airfoils," AIAA Paper 94-0050, Jan. 1994.

[8]Mani, M., and Bush, R. H., "Overlapping Grid Method for High-lift and Store Carriage Applications," AIAA Paper 93-3428, Aug. 1993.

[9]Mathias, D. L., "Navier-Stokes Analysis of the Flow About a Flap Edge," M.S. Thesis, Aeronautical Engineering Dept., California Polytechnic State Univ., San Luis Obispo, CA, 1994.

[10]Mathias, D. L., Roth, K. R., Ross, J. C., Rogers, S. E., and Cummings, R. M., "Navier-Stokes Analysis of the Flow About a Flap Edge," AIAA Paper 95-0185, Jan. 1995.

[11]Hicks, R. M., and Schairer, E. T., "Effects of Upper Surface Modification on the Aerodynamic Characteristics of the NACA 63_2-215 Airfoil Section," NASA TM 78503, Jan. 1979.

[12]Storms, B. L., and Ross, J. C., "Aerodynamic Influence of a Finite-Span Flap on a Simple Wing," Society of Automotive Engineers, Paper 95-1997, Warrendale, PA, Sept. 1995.

[13]Storms, B. L., and Ross, J. C., "An Experimental Study of Lift-Enhancing Tabs on a Two-Element Airfoil," AIAA Paper 94-1868, June 1994.

[14]Rogers, S. E., "Numerical Solution of the Incompressible Navier-Stokes Equations," NASA TM 102199, Nov. 1990.

[15]Rogers, S. E., and Kwak, D., "Upwind Differencing Scheme for the Time-Accurate Incompressible Navier-Stokes Equations," *AIAA Journal*, Vol. 28, No. 2, 1990, pp. 253–262.

[16]Chorin, A. J., "A Numerical Method for Solving Incompressible Viscous Flow Problems," *Journal of Computational Physics*, Vol. 2, No. 1, 1967, pp. 12–26.

[17]Roe, P. L., "Approximate Riemann Solvers, Parameter Vectors, and Difference Schemes," *Journal of Computational Physics*, Vol. 43, No. 2, 1981, pp. 357–372.

[18]Baldwin, B. S., and Barth, T. J., "A One-Equation Turbulent Transport Model for High Reynolds Wall Bounded Flows," AIAA Paper 91-0160, Jan. 1991.

[19]Rogers, S. E., Menter, F. R., Durbin, P. A., and Mansour, N. N., "A Comparison of Turbulence Models in Computing Multi-Element Airfoil Flows," AIAA Paper 94-0291, Jan. 1994.

[20]Benek, J. A., Buning, P. G., and Steger, J. L., "A 3-D Chimera Grid Embedding Technique," AIAA Paper 85-1523, July 1985.

[21]Tramel, T. W., and Suhs, J. L., "PEGSUS 4.0 User's Manual," Arnold Engineering Development Center, TR-91-8, Arnold Air Force Station, TN, June 1991.

Color reproductions courtesy of NASA Ames Research Center.